Low-temperature charging of lithium-ion cells part I: Electrochemical modeling and experimental investigation of degradation behavior

CrossMark

Simon Tippmann [a],*, Daniel Walper [a], Luis Balboa [a], Bernd Spier [a], Wolfgang G. Bessler [b]

[a] Deutsche ACCUmotive GmbH & Co. KG, Neue Str. 95, 73230 Kirchheim, Teck, Germany
[b] Offenburg University of Applied Sciences, Institute for Energy System Technology, Badstr. 24, 77652 Offenburg, Germany

HIGHLIGHTS

- Parameterization and validation of an electrochemical model over a wide temperature range.
- Obtainment of model parameters via piecewise investigation of electrochemical impedance spectroscopy (EIS) data.
- Experimental data of low temperature degradation behavior of full cells.
- Correlation of electrochemical model and experimental data regarding low temperature degradation behavior (Li-plating).
- Introduction of a semi-quantitative degradation factor related to the local anode potential.

ARTICLE INFO

ABSTRACT

Fast charge of Li-ion cells is one of the main challenges in automotive battery application. As a particular problem at low temperatures and high charging rates, lithium deposits as metal on the anode surface (so-called lithium plating) instead of intercalation. Electrochemical models help to understand internal processes and predict aging effects, which finally lead to optimized charging strategies. In this work, a 1D + 1D (pseudo-2D) electrochemical model is developed, applied over a wide range of temperature ($T = -25$ °C to 40 °C) and current ($I = 0.1$ C to 6 C), and coupled with a 0D thermal model. The model is parameterized with measurement data in frequency domain using electrochemical impedance spectroscopy (EIS) and validated with time-domain data. In experiments cells are charged under different operating conditions. Capacity fade is measured after a significant number of cycles and compared to the simulated anode potential. A qualitative correlation is found between the degradation in experiment and the anode potential dropping below 0 V vs. Li/Li$^+$ at the separator-anode boundary in the simulation. Furthermore a semi-quantitative expression for degradation is introduced. The transformation of the model into an on-board applicable form is presented in the companion contribution (part II).

© 2013 Elsevier B.V. All rights reserved.

1. Introduction

Li-ion batteries have been extensively studied in the past years, both in experiment and modeling. For previous applications like consumer electronics, thermal behavior has been sufficiently considered around room temperature. Therefore, also the focus of modeling activities has been between 25 °C and 40 °C. As Li-ion chemistry recently became the favorite technology for use in traction batteries for electrical and hybrid vehicles, operation of cells has to be ensured in a wide temperature range and simultaneously has to meet the lifetime requirements for automotive purposes under these environmental conditions. Understanding

the limiting factors for operation at low temperatures in terms of power and energy capability, e.g., cold cranking power, becomes one target for cell and battery suppliers and has been recently addressed in simulations by Ji et al. [1].

Not only the electrical performance has to be taken into account, also aging behavior at extreme thermal conditions has to be understood well to extend lifetime and performance to a maximum. Rapid charging is one of the main challenges in battery research and gets even more challenging at subzero temperatures due to the limited kinetics of electrochemical systems. Under these conditions lithium deposits in an unwanted side reaction on the anode surface instead of intercalating in the anode particles. This so-called lithium plating leads to capacity loss, which affects lifetime dramatically. Metallic lithium is highly reactive and is assumed to react quickly with the electrolyte components to form insoluble products leading to an increase of the passivation layer on the

---

anode surface and electrolyte depletion. Dendritic growth of metallic lithium has also been reported [2]. Dendrites are a potential safety hazard by penetrating the separator and causing an internal soft-shortening of the cell. This is also why lithium metal anodes are avoided in consumer cells despite their promising potential in power and energy density [3].

Electrochemical models are crucial in understanding internal processes, e.g., degradation effects. The design process of batteries can be supported as well as derivation of optimized operation conditions. Concentrated solution and porous electrode theory introduced by pioneers Newman and coworkers [4–6] have become the widely used principles and acclaimed theory in literature [7] which also found their way into commercial tools like COMSOL Multiphysics which is used in this study.

The parameterization of electrochemical models is one of the problematic key factors of building up a reliable model because of the large number and sensitivity of parameters as well as their frequently unknown dependencies on temperature and Li-concentration. Literature values often strongly vary for the same materials due to different measurement techniques. Few papers have been published presenting a full set of characterized material properties. Hence, there are several different mathematical parameterization methods presented by obtaining material parameters of electrical measurements from the full cell instead of directly measure material properties. Physical model reduction, namely single-particle model (SP-model), allows for time-efficient calculations as well as parameterization techniques and has recently also been extended by a thermal energy balance [8,9]. By neglecting local current distribution in this approach such a model can only be used for low C-rates and small electrode thickness. A promising reformulated mathematical model is presented in Ref. [10] for real-time parameter estimation but has only been validated for rates up to 2 C and few input parameters. Experiment-driven parameterization of electrochemical models combined with fitting algorithms is presented in Refs. [11,12] by incorporating time domain data, respectively discharge–charge profiles. A more sophisticated but also more complex approach is the support of 1D models by extracting effective parameters of 3D structure resolved models as presented in Ref. [13].

First modeling approaches of Li-plating have been made by Arora et al. [14] resulting in an understanding of the lithium deposition reaction by extension of an electrochemical model. In that work lithium plating has been assumed as overcharge reaction which is likely to happen outside the defined voltage limits only not taking into account any temperature dependencies. Lithium deposition is often observed taking place at electrode edges due to non-uniformity of current and temperature distribution and design parameters. A 2D-modeling approach for studying edge effects is presented in Ref. [15]. Modeling the complexity of the solid electrolyte interphase (SEI) [16] growth which is clearly linked to Li-deposition reaction has been addressed by several research groups [17–20]. Experimental work on micro-structure level and visualization of lithium dendrite growth are presented by Harris [2]. Experimental work on the influence of electrolyte properties with regard to lithium plating is described in Ref. [21].

Given this situation this contribution presents a fully parameterized electrochemical model over a wide temperature and current range for a large-format high-energy automotive lithium-ion cell. The model has been linked with a thermal model which is essential for operation at low temperatures due to strong heating under load. Parameterization has been conducted via piecewise investigation of electrochemical impedance spectroscopy (EIS) measurement data of the full cell. Different operation parameters like charging current, cut-off voltage, temperature, and initial SOC are studied on a wide range in order to detect increased aging

effects due to Li-plating. The validated model is used for predicting the lithium deposition reaction at low temperature charging and compared to experimental degradation measurements. A semi-qualitative approach is introduced for expressing the level of degradation. Part II [22] of the paper presents a novel transformation of the model into an online-applicable form which can easily be integrated into a battery management system (BMS) while allowing to control internal cell parameters.

2. Methodology

2.1. Studied cells

In this work a high-energy Li-ion cell consisting of a graphite anode and NMC cathode was studied. Design parameters and electrochemical properties are listed in Table 1. Electrochemical performance parameters of the full cell are determined by an experiment-driven parameterization technique which is introduced in Section 4.2.

2.2. Experiments

Electrical tests were performed within the limits of 3.0 V for the lower and 4.2 V for the upper cut-off-voltage. Charging was performed with a constant current (CC) until reaching the upper voltage and is followed by a constant voltage (CV) phase until the current drops below a specific value. As break criteria for the CV phase $I < C/20$ has been chosen. For discharging only CC was used until reaching the end voltage. Experiments were done in Vötsch climate chambers and tests were controlled by BaSyTec systems and measurement data recorded in BaSyTec software. GAMRY instruments were used for measuring electrochemical impedance spectroscopy (EIS) in galvanostatic mode.

Temperature profiles were measured with PT100 sensors. For low discharge rates ($I < 1$ C) one sensor was placed in the middle of the cell area. For higher rates also temperature gradient was determined by six sensors on the cell area. When plotting temperature rise, a mean value is shown.

For degradation measurements, 1 C constant current discharge was performed for determining capacity of the cells before and

Table 1
Design adjustable parameters and electrochemical properties for the investigated Li-ion cell.

Parameter	Anode	Separator	Cathode
Thickness L [μm]	65[a]	28[a]	54[a]
Porosity ε_s	0.62[a]	0.52[a]	0.49[a]
Particle radius r [μm]	10[a]	–	10[a]
Electrolyte concentration c_l [mol m^{-3}]	–	1100[a]	–
Maximum theoretical concentration c_s^{max} [mol m^{-3}]	31,363[b]	–	51,385[b]
Electric conductivity σ_{cond} [S m^{-1}]	0.4[b]	–	100[b]
Ionic conductivity κ_l [S m^{-1}]	–	Table 3[c]	–
Reaction rate k [m s^{-1}]	Table 3[c]	–	Table 3[c]
Charge transfer coefficient α	0.5[b]	–	0.5[b]
Thermodynamic factor ν_l	–	Table 3[c]	–
Transference number t_+^0	–	0.363[b]	–
Diffusion coefficient D [m^2 s^{-1}]	Table 3[c]	Table 3[c]	4×10^{-11}
Double layer capacity C^{dl} [F m^{-2}]	Table 3[c]	–	Table 3[c]
Cell density ρ_{cell} [kg m^{-3}]	2976[a]		
Heat capacity c_p [J kg^{-1} K^{-1})]	1090[a]		
Emissivity factor ε	0.96[b]		
Convective heat transfer coefficient h [W m^{-2} K^{-1})]	8.7[b]		

[a] Measured.
[b] Assumed.
[c] Fitted.

after low-temperature charging cycles. Tests were performed for different cells with CC charging and for several tests with a subsequent CV charge. As the energy and charge throughput varies for different temperatures, currents, voltage limits and aging conditions, capacity fade with discharge capacity before $Q_{dis,1}$ and after $Q_{dis,2}$ is normalized by the total charge throughput $Q_{char,tot}$ for all low temperature cycles. The degradation can then be expressed as:

$$\theta^{norm} = \frac{(Q_{dis,2} - Q_{dis,1})/Q_{dis,1}}{Q_{char,tot}}. \tag{1}$$

To gain knowledge of the degradation behavior at fixed temperatures and without evaluating thermal effects, heat removal has to be ensured to a maximum during the electrical tests. Therefore additional fans were used for the air recirculation to achieve a quasi-isothermal measurement in the climate chambers. During low-temperature cycling, the cell was discharged with a relatively moderate discharge rate of C/2 to prevent additional aging effects at discharge. As it is nearly impossible to determine the amount of plated lithium in a full cell, capacity fade is used here as correlation for irreversible lithium deposition. It should be mentioned that 1 C discharge capacity often used in battery development for calculating nominal capacity is no intrinsic quantity. A rise in ohmic resistance also leads to a smaller capacity. As all degradation is assumed to take place because of lithium plating reaction, the real capacity loss and rise in ohmic resistance was not separated in study. Nevertheless, for low temperature cycles performed in this study, a rise in ohmic resistance can be interpreted as SEI-layer growth due to the presence of highly reactive metallic lithium. Decomposed electrolyte molecules react with lithium to form insoluble products which will become part of the SEI and lead to an increase of the inner resistance of the cell.

2.3. Simulations

COMSOL Multiphysics 4.2 and the integrated Battery & Fuel Cells Module are used to perform simulations. For better control of the input parameters and the implementation of an optimization algorithm, the model is live linked with MATLAB. For realizing CV charging an event controller is integrated in the model which allows management of all internal parameters, mainly used for current and voltage, similar to a BMS. Table 2 lists the approximate simulation times for the performed studies. When simulating real driving profiles the time stepping had to be set to 0.1 s to achieve reliable results. All times are listed for a fixed time step of 1 s. The mesh used in this study has 101 grid points in layer and 11 points in particle radius direction.

3. Electrochemical and thermal model

The model represents a lithium-ion battery consisting of two porous electrodes insulated by a separator in a liquid electrolyte. During discharging, Li-ions, which are intercalated in the graphene

Table 2
Comparison of simulation times for different studies and model set-ups.

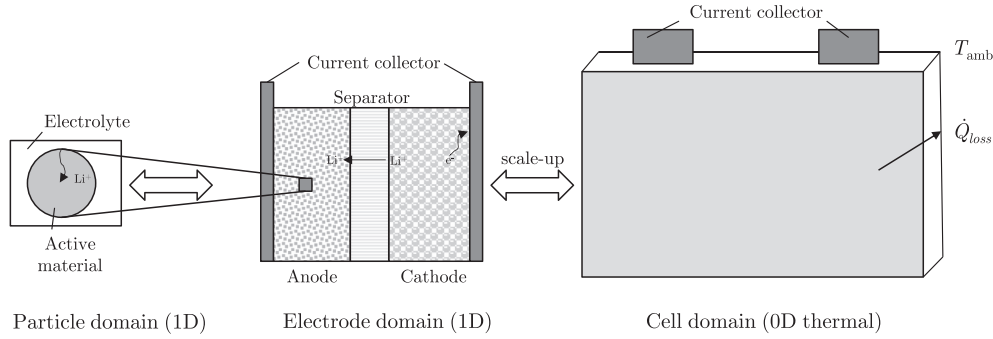| Case	Time
1 C discharge at 25 °C	~60 s
1 C discharge with thermal model at 25 °C	~100 s
1 C discharge with electrochemical BMS at 25 °C	~70 s
1 C discharge with thermal model and electrochemical BMS at 25 °C	~120 s
Impedance study at 25 °C	~30 s
Driving profile 10 min at 25 °C	~30 min

layers of the graphite anode, move through the electrolyte and the separator to the cathode side. Li-ions diffuse in the lattice of the host electrode material. Charging inverts the direction in which the lithium ions and the electrons move. Differential equations first established by Newman and coworkers [4–6] describing this electrochemical system are used in this contribution (1D + 1D) and are coupled with a 0D thermal model according to [23,24]. The model equations from literature for both the electrochemical and the thermal model are summarized in the following. All symbols used in the equations are listed in Appendix A. Fig. 1 shows the model domains schematically.

3.1. Electrochemical model

The following PDEs are solved for the dependent variables spatially in the electrode layer and for the bulk diffusion in particle radius direction. For spherical particles, the diffusion is described by Fick's second law:

$$\frac{\partial c_s}{\partial t} = \frac{1}{r^2}\frac{\partial}{\partial r}\left(D_s r^2 \frac{\partial c_s}{\partial r}\right). \tag{2}$$

The potential in the solid active material is calculated by Ohm's law:

$$i_s = -\sigma_{cond}\nabla\phi_s. \tag{3}$$

Electrolyte potential is expressed as

$$\nabla\phi_l = -\frac{i_l}{\kappa_l} + \frac{2\,RT}{F}\left(1 - t_+^0\right)\left(1 + \frac{d\ln f_\pm}{d\ln c_l}\right)\nabla\ln c_l. \tag{4}$$

For simplification of parameterization, the symbol ν_l is used for the following expression:

$$\nu_l = \left(1 - t_+^0\right)\left(1 + \frac{d\ln f_\pm}{d\ln c_l}\right). \tag{5}$$

Mass balance under consideration of porous electrode and concentrated solution theory writes as

$$\varepsilon_l\frac{\partial c_l}{\partial t} = \nabla\varepsilon_l D_l\nabla c_l + \frac{\nabla i_l}{F}\left(1 - t_+^0\right). \tag{6}$$

For porous media the effective transport properties are calculated using Bruggeman correlation. The coupling at the solid/liquid interfaces, which represents the electrochemical reaction rate in dependency of the concentration and the local overpotential, is described by the Butler–Volmer equation:

$$i_{loc} = i_0\left[\exp\left(\frac{\alpha_a F\eta}{RT}\right) - \exp\left(\frac{-\alpha_c F\eta}{RT}\right)\right]. \tag{7}$$

The activation overpotential is defined as the difference between the potentials in liquid and solid and a potential drop over the SEI-layer referred to the open circuit potential of the electrode materials

$$\eta = \phi_s - \phi_l - \phi^0 - \Delta\phi_{Film}. \tag{8}$$

For the exchange current density, the following concentration dependent form is chosen in this work:

$$i_0 = F(k_a)^{\alpha_c}(k_c)^{\alpha_a}\left(c_s^{max} - c_s\right)(c_s)^{\alpha_a}\left(\frac{c_l}{c_l^{ref}}\right). \tag{9}$$

Current balance writes as

$$\nabla i_s + \nabla i_l = 0, \tag{10}$$

Fig. 1. Schematic illustration of modeling domains.

with

$$\nabla i_l = \sum_i a_i^V i_{\text{loc},i} + a^{\text{dl}} C^{\text{dl}} \frac{\partial(\phi_s - \phi_l)}{\partial t} \tag{11}$$

due to the assumption of the presence of a double layer with capacitance C^{dl}.

3.2. Thermal model

The electrochemical model is extended by 0D a thermal model. Ohmic heat is calculated using

$$\dot{q}_{\text{ohm}} = \sigma_{\text{cond}} \nabla \phi_s \nabla \phi_s + \kappa_l \nabla \phi_l \nabla \phi_l + \frac{2\kappa_l RT}{F}\left(1 - t_+^0\right)\left(1 + \frac{\text{d}\ln f_\pm}{\text{d}\ln c_l}\right). \tag{12}$$

Heat released due to the electrode reaction is given by

$$\dot{q}_{\text{reac}} = a^V i_{\text{loc}} \eta. \tag{13}$$

An entropy change in consequence of the electrode reaction results in a reversible heat and can be expressed with the temperature-dependent open circuit potential

$$\dot{q}_{\text{rev}} = a^V i_{\text{loc}} \frac{\partial \phi^0}{\partial T}. \tag{14}$$

The heat balancing equation is used to calculate the temperature rise:

$$\rho_{\text{cell}} V_{\text{cell}} c_p \frac{\partial T}{\partial t} = A_e \int_0^L (\dot{q}_{\text{ohm}} + \dot{q}_{\text{reac}} + \dot{q}_{\text{rev}}) \, \text{d}L - \dot{Q}_{\text{loss}}. \tag{15}$$

For the heat loss, radiation and convection are considered:

$$\dot{Q}_{\text{loss}} = 2h A_{\text{cell}}(T - T_{\text{amb}}) + 2\sigma_{\text{Boltz}} \varepsilon A_{\text{cell}}\left(T^4 - T_{\text{amb}}^4\right). \tag{16}$$

4. Model parameterization and validation

In this section a temperature-dependent parameterization of the aforementioned model equations with the help of a large set of frequency-domain data is introduced. The estimated parameter sets are then validated by comparing time-domain measurements.

Literature values for the electrode materials often vary over several orders of magnitude. For the commercial cells used in this study, many electrochemical properties are unknown and have to be estimated.

4.1. Half-cell potentials and electrode balancing

Kumaresan et al. [25] provide a method to link the initial state of charge of the cell with the stoichiometric coefficients of the electrodes. Open circuit potentials (OCPs) of both electrode materials are fitted against quasi-static discharge curves at 25 °C. For the OCPs a best fitting approach is used with rational functions:

$$\phi_{\text{an}}^0 = \frac{\left(-2137\psi^3 + 1841\psi^2 + 107.44\psi + 12.85\right)}{\left(\psi^4 - 15113\psi^3 + 16128\psi^2 + 436.68\psi + 10.71\right)}, \tag{17}$$

$$\phi_{\text{cat}}^0 = \frac{\left(-3249\xi^3 + 10789\xi^2 - 9090\xi + 2929\right)}{\left(\xi^4 - 532\xi^3 + 2088\xi^2 - 1767\xi + 587\right)}. \tag{18}$$

Variables ψ and ξ express a dimensionless concentration c_s / c_s^{max}. Characteristic points in the measurement of the full cell can also be seen in half cell potential and offer information about the electrode balancing. Applying this method gives the following relationship between the solid concentration c_s and the cell's SOC,

$$c_{\text{an}}^{\text{ini}} = \left(\text{SOC}^{\text{ini}}(\psi_{100\%} - \psi_{0\%}) + \psi_{0\%}\right) c_{\text{an}}^{\text{max}} \tag{19}$$

$$c_{\text{cat}}^{\text{ini}} = \left(\text{SOC}^{\text{ini}}(\xi_{100\%} - \xi_{0\%}) + \xi_{0\%}\right) c_{\text{cat}}^{\text{max}} \tag{20}$$

with the elaborated values for 0% and 100% cell SOC respectively:

$$\psi_{0\%} = 0.07; \quad \psi_{100\%} = 0.61$$

$$\xi_{0\%} = 0.98; \quad \xi_{100\%} = 0.48$$

The successful parameterization of thermodynamic properties is the basis for further procedure.

4.2. Parameterization (frequency domain)

Frequency analysis, respectively electrochemical impedance spectroscopy (EIS), allows to separate different internal processes and has been widely used for estimation of parameters for semi-physical equivalent circuit models. Simulations in frequency domain, which are based on a linearization of the equations at a given point similar to the descriptions in Refs. [26], are performed in COMSOL's frequencies study. Another positive effect of simulations in frequency domain is the fact that computation is much faster, which facilitates the whole parameterization process (Table 2). The kinetic parameters of the cell are worked out by piecewise investigation of the measurement data. Bulk diffusion coefficients for NMC have been reported more than one order of

magnitude higher than diffusion coefficients for Li$^+$ in the graphene layers of the anode (cf. Ref. [27,28]). Hence, the cell behavior is limited by the anode and electrolyte properties underlying same particle sizes for the anode and cathode active material. Diffusion at the cathode side is then approximated with a constant value of $D_{cat} = 4 \times 10^{-11}$ m^2 s^{-1} for the whole temperature range.

Galvanostatic EIS which measures a voltage response to an alternating current with an amplitude of C/50 over a frequency range from 5 kHz to 10 mHz has been performed for the full cell. Inductive behavior is neglected when simulating the frequency response. To elaborate the temperature as well as the concentration dependencies of the parameters, measurements have been performed from 40 °C down to −25 °C in steps of 5 °C and from 100% to 0% SOC in steps of 10%. For selected temperatures, the frequency range has been enlarged down to 1 mHz which becomes important for visualizing low-temperature diffusion processes. Fig. 2 shows the Bode plot of an EIS measurement for a Li-ion cell exemplarily for 25 °C and 20 °C, and the independently determined parameters.

For obtaining initial parameters as well as upper and lower bounds for the fitting algorithm, a comprehensive sensitivity analysis for each parameter was performed in advance. The following parameters were determined to be the most sensitive to reproduce temperature dependent cell behavior:

- D_{an} — bulk diffusion coefficient of Li$^+$ in anode (cf. Eq. (2))
- D_l — diffusion coefficient of Li$^+$ in the electrolyte (cf. Eq. (6))
- ν_l — thermodynamic factor of the electrolyte (cf. Eqs. (4) and (5))
- k_{an} — reaction rate constant of anode (cf. Eq. (9))
- k_{cat} — reaction rate constant of cathode (cf. Eq. (9))
- C_{an}^{dl} — double layer capacity of anode (cf. Eq. (11))
- C_{cat}^{dl} — double layer capacity of anode (cf. Eq. (11))
- κ_l — ionic conductivity of the electrolyte (cf. Eq. (4))

For parameter estimation a Nelder−Mead method [29] has been proven to be the most stable even though the speed is inferior compared to other algorithms. For minimization, a weighted chi-square function χ^2 is used which not only incorporates total errors but also errors of the gradient. Thus, the algorithm is forced to keep the trend and shape of the target values. The error function is expressed as follows:

$$\chi^2 = \omega_1 \sum_i^N \left(\frac{y_i - f(x_i)}{\sigma_i} \right) + \omega_2 \sum_i^N \left(\frac{(dy_i - df(x_i))/(df)}{\sigma_i'} \right). \quad (21)$$

Weighting the gradient function against the absolute error function, the factors ω_1 and ω_2 are used. σ_i and σ_i' express the standard deviations of the measurement data. The fitting algorithm is first performed individually for each temperature at a fixed SOC of 50%. Solutions of local minimums are avoided by a random use of starting parameter for a significant number of runs in between the chosen boundaries. Under the assumption that the temperature dependency of the parameters can be expressed with an exponential Arrhenius equation behavior

$$A = A_0 \cdot \exp(-E_a/RT), \quad (22)$$

parameters are also fitted individually in a second step for the whole temperature range. In this case, the pre-exponential factor A_0 and the activation energy E_a are determined for each of the aforementioned parameters. Combining these two steps leads to a full set of parameters best suited for the temperature range which can be transformed into consistent analytical functions (Table 3). Trend functions for the electrolyte properties κ_l, ν_l and D_l are mainly based on the achievements made by Valoen and Reimers [30] who have presented a full set of temperature and concentration dependent smoothing functions for a LiPF$_6$ PC/EC/DMC mixture. Fig. 3 shows the simulation results in comparison to measurement data for temperatures of 25 °C and 10 °C as well as 0 °C and −15 °C for a frequency range from 1 kHz to 10 mHz. Considering the impedance rise of two orders of magnitudes for the plotted curves, the simulation yields consistently good fits.

Comparing different SOCs (here 10% and 90%) at a temperature of 0 °C shows also plausible results (Fig. 3c). For smaller SOCs, the impedance rises for lower frequencies in the real part and for frequencies around 1 Hz in the imaginary part of the complex resistance.

4.3. Validation (time domain)

As simulation results in frequency domain are in agreement and consistent with measured values over a wide range, also discharging and charging processes observed in the time domain have to be in agreement for the adopted parameters. Therefore, measured discharge curves with rates up to 6 C and temperatures down to −20 °C are compared to simulated curves. For high current discharge and low temperature operation, a thermal model is essential due to measured temperature rises of about 50 °C in one discharge cycle. Also entropy effects of the electrodes have to be taken into account as the measured temperature rise could not be
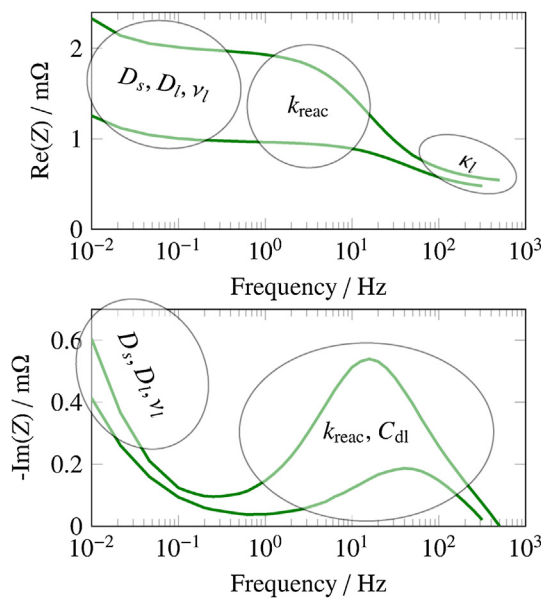

Fig. 2. Bode diagram with schematic illustration of parameters for temperature-dependent parameterization of the model at measurement data of 25 °C (lower curve) and 20 °C (upper curve).

Table 3
Fitted model parameters as function of electrolyte concentration c_l in mol m^{-3} and temperature T in K.

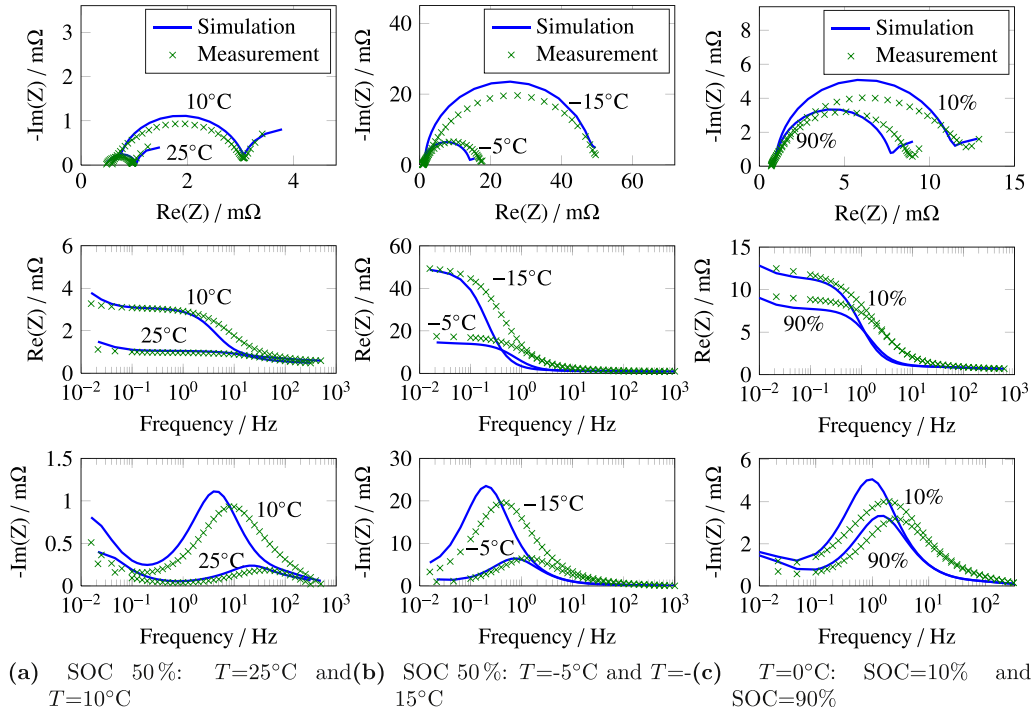| Parameter	Function	Unit
D_{an}	$1.87 \cdot 10^{-8} \cdot \exp(-3936/T)$	m^2 s^{-1}
C_{an}^{dl}	0.92	F m^{-2}
C_{cat}^{dl}	80.23	F m^{-2}
k_{an}	$1178 \cdot \exp(-9237/T)$	m s^{-1}
k_{cat}	$3.6 \cdot \exp(-9616/T)$	m s^{-1}
D_l	$1.81 \cdot 10^{-8} \cdot \exp(-0.55\, c_l/1000) \cdot \exp(-1178/T)$	m^2 s^{-1}
ν_l	$2.95 \cdot 10^{-3} \cdot \exp(-1720/T)$	
κ_l	$1185 \cdot (c_l/1000)^{-0.1882} \cdot \exp[-0.9615 \log(c_l/1000)^2] \cdot$ $\exp(-2098/T)$	S m^{-1}

Fig. 3. Comparison of experimental and simulated impedance spectra for different temperatures and SOCs.

reconstructed without applying a temperature dependent open circuit potential. Open circuit voltage (OCV) measurements for the full cell performed at different temperatures are used to work out the dependence. A strong influence of the state of charge on the temperature derivative of the OCV was found which has also been reported in Ref. [24]. As it is difficult to separate these effects for both electrodes, the reversible heat is completely ascribed to the cathode. The temperature dependence of the open circuit potential is incorporated with a 4th degree polynomial smoothing function in the following form:

$$\frac{\partial \phi_{cat}^0}{\partial T} = 0.0620\xi^4 - 0.1913\xi^3 + 0.2133\xi^2 - 0.1022\xi + 0.0179 \tag{23}$$

Fig. 4 shows a full set of simulated discharge curves together with the measurements. All cells were fully charged to 100% with a CC/CV method and a rest period of about one hour. Discharge curves were performed until the cut-off voltage of 3 V is reached with a subsequent relaxation phase. Good agreement can be seen

for a variation of C-rates at a fixed temperature of 0 °C. Considering temperature rise and sensitivity of the parameters, the coupled thermal-electrochemical model gives good results for voltage as well as temperature profiles.

For discharge rates smaller than 0.5 C, only small temperature rises were measured and temperature effects on the electrochemical parameters are minor, which can also be seen in the simulations. Varying current and temperature for rates below 1 C also shows good agreement, even though the voltage is slightly overestimated (Fig. 5). Especially at low SOCs, the curve is shifted which can be explained by not incorporating a concentration-dependent bulk diffusion coefficient on the anode side. Coefficients for graphite have been reported to vary in large order over the stoichiometric coefficients [28]. The model delivers reasonable and plausible behavior for all simulations performed in the parameterized temperature range.

As the work focuses on automotive application, more dynamic profiles have to be considered during operation. Fig. 6 shows a 10 min section of the voltage response of an urban city driving profile at 15 °C. Even though the computing time is substantial (cf.
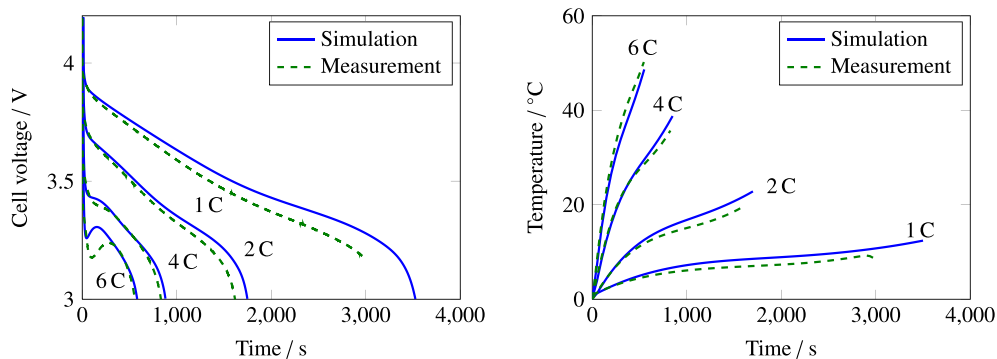

Fig. 4. Comparison of experimental and simulated discharge curves and temperature profiles for different discharge rates at 0 °C.
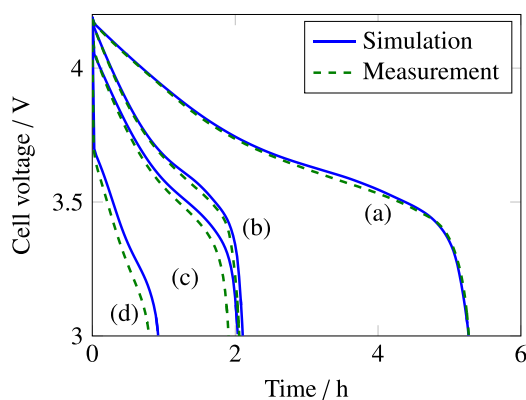
Fig. 5. Comparison of experimental and simulated discharge curves for small C-rates (a) 25 °C, 0.2 C, (b) 40 °C, 0.5 C, (c) 10 °C, 0.5 C, (d) −10 °C, 1 C.

Table 2) compared to equivalent circuit models which are state of the art for such simulation requests, the model gives promising results with a root mean square error of 15 mV and a maximum error of 40 mV.

Relying on the results of the time domain validation, it is well assumed that internal parameters are also predicted correctly. For a more in depth experimental validation a broad study with half cells would be required although spatial dependencies are hard to measure. Validation of such a model facilitated by measurement data of a three electrode cell can be found in Ref. [31].

5. Degradation experiments

In this section, the experimental results of degradation measurements are discussed. To explore the degradation behavior, cells were charged at different temperatures and operational parameters. Capacity fade was then measured at room temperature after low-temperature cycles.

Fig. 7 shows a binary image of the normalized degradation θ^{norm} for the tested cells over temperature and current.

The tested cells were charged for multiple cycles with a CC charge phase up to a maximum of 4.05 V, a relaxation period of at least 30 min, a discharge rate with C/2 and a second relaxation period of 30 min. Due to kinetic inhibition, especially diffusion of Li$^+$ in electrolyte and bulk diffusion the degradation increases with lower temperature. For the highest currents tested, the degradation decreases which can be explained by the following points:

1. High internal temperature rise due to high currents which cannot be measured outside the cell;

2. Early reach of cut-off voltage and lack of constant voltage phase, therefore no concentration build-up at particle surface which possibly leads to degradation.

The second point has also been reported by Kwon et al. [32,33] which is named critical charge capacity in their work. They proposed that only a specific capacity can be charged with a given current at a given temperature. A detailed model view and simulation results of this behavior are given in Section 6.

Results which support this assumption are illustrated in Fig. 8.

Charging current is plotted against the charged capacity for the currents at a temperature of −15 °C. Red crosses mark the tests for which a significant capacity fade has been determined and blue circles represent tests without aging. Separating the points by a trendline gives the assumed critical charge capacity. For these tests different cells have been charged partially. It can be observed that even if the charging current is high no capacity loss is measured if the charged capacity is below a non-harming critical value. Using the same current for the full voltage or SOC range leads to increased aging. All the cells have initially been in a fully equilibrated or relaxed state. For the cells partially charged the concentration gradient and particle surface concentration seems not to exceed some critical value which favors the lithium plating reaction, even when the state of charge is high, which means anode concentration is near a possible maximum, and lithium deposition is more likely to happen. Fig. 9 illustrates this theory schematically.

6. Simulation study

In this section, the validated model is used to analyze and illustrate the low-temperature charging behavior and the degradation effects observed in the experiments. Different operational parameters are studied by varying the initial parameters of the model and evaluating the results for a large set of simulations graphically in degradation maps.

6.1. Visualization of spatially resolved low temperature concentration distribution

First, the derived model is used to support the theoretical considerations illustrated in Fig. 9. Therefore, a full cycle is simulated at 0 °C and the concentration distribution is visualized spatially (Fig. 10).

The cycle starts at 100% SOC, i.e., with a lithiated anode and a delithiated cathode. Discharge is performed with 1 C followed by a relaxation period of 1 h. Afterward, CC/CV charging with a rate of 1 C and a minimum current of C/20 for CV charging is applied and followed by a relaxation phase. For visualization, the concentration is normalized and calculated as electrode SOC individually for each
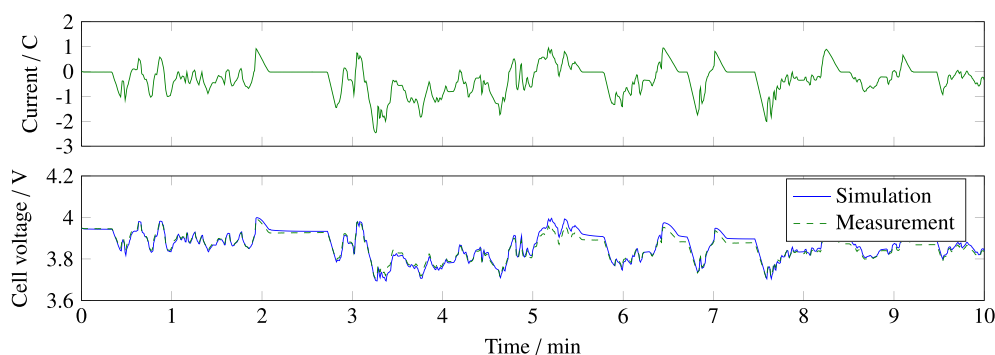

Fig. 6. Comparison of experimental and simulated voltage profile for an urban city driving profile at 15 °C.
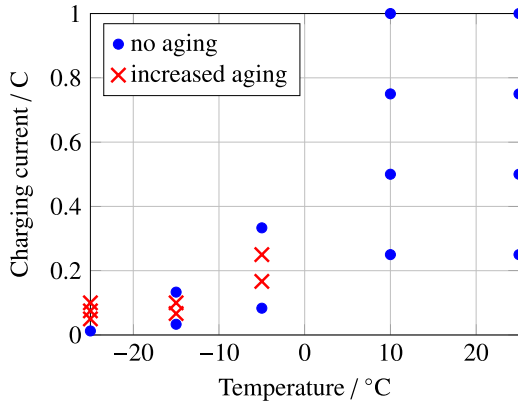
Fig. 7. Experimental degradation for CC charging to 4.05 V over temperature and current range.

electrode by replacing SOC^{ini} in Eq. (19) for the anode and Eq. (20) for the cathode with the following expressions respectively:

$$SOC^{ini} = SOC_{an};\tag{24}$$

$$SOC^{ini} = 1 - SOC_{cat}.\tag{25}$$

The profile shows the normalized concentration distribution in the porous electrode (1D) as well as in dimensionless radial direction r_i/r in the particles (+1D) for different points in time during the cycle. The dimensionless radius $r_i/r = 1$ is equivalent to the particle surface while $r_i/r = 0$ represents the particle center. The panels on top show the current, the terminal voltage of the cell, and the anode potential at the anode-separator boundary.

At end of CC discharge (Fig. 10a), while the anode-separator boundary is fully delithiated, Li is still present in areas near the current collector. Due to the faster bulk diffusion processes in comparison to the anode, nearly no gradient can be seen in the cathode.

At end of CC charge (Fig. 10b), the plot shows the transition from CC to CV phase, more precisely the end of constant current charge at 4.2 V. An enormous concentration gradient is built up in the anode layer. The cell is partially overcharged at the particle surfaces while other parts are still delithiated. Such behavior cannot only be seen at the end of the charge process, but also soon after applying the charging current although the terminal voltage has not yet reached the cut-off voltage by far. The higher the charging current
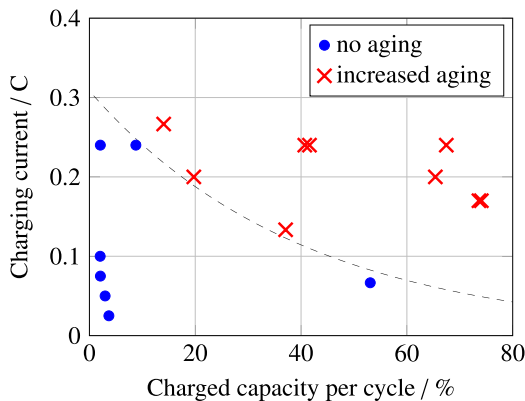

Fig. 8. Experimental results of no aging and increased aging for different charge capacity at −15 °C. The trendline is a guide to the eye.

and the lower the temperature, the faster the concentration build-up takes place, which finally leads to increased aging as the cell is partially overcharged.

At end of relaxation after CV charge (Fig. 10c), in this special case, the CV phase has taken multiple hours and more than double of the time of the CC phase. The anode seems to be equilibrated, but there is still a gradient of about 25% SOC from the center of the particles near the current collector to particles next to the separator.

Concentration accumulation is also expressed in the local potential which can be seen in the curve for ϕ_{an} in Fig. 10. It is well known that the local potential dropping below 0 V vs. Li/Li$^+$ leads to metallic lithium to be formed [14]. The lithium deposition reaction then becomes favorable over the intercalation in graphene layers.

6.2. Degradation analysis

In the following a semi-qualitative correlation of degradation with the anode potential is introduced and the results are compared to the degradation experiments. Using the one-dimensional approximation, the potential during the charging process is always lowest at the anode-separator boundary, and aging predominantly takes place there. The model is therefore used for investigation of operational parameters and development of an optimized non-harming charging strategy. To work out the relationship between current, temperature and anode potential (respectively lithium plating) charging simulations were performed from 1 C down to 0.1 C with a subsequent CV phase in a temperature range from −20 °C to 25 °C and different initial SOCs.

Results for the anode potential at 0 °C for different charging currents are shown in Fig. 11. The simulations are performed with and without a thermal model. For the isothermal calculations the potential drops below 0 V vs. Li/Li$^+$ for currents down to 0.2 C which is in good agreement with the quasi-isothermal measured degradation values in Section 5.

For thermal calculations, higher currents lead to higher temperature rises and potential curves tend to rise because of increased kinetics due to their temperature-dependency (Fig. 11b). In comparison to the isothermal behavior the absolute values of the anode potential change significantly for high charging rates. The amount of deposited lithium can be qualitatively described using the following assumption:

$$\Theta_I = \int_{\phi_{s,a<0}} I \, dt.\tag{26}$$

As the charged capacity differs for the applied currents and temperatures, the degradation factor Θ is normalized to the total charge according to:

$$\Theta_I^{norm} = \frac{\Theta_I}{\int I \, dt}.\tag{27}$$

The normalization becomes especially important when comparing partial charges to a given voltage (cf. Fig. 7).

For a complete cycle with a CV phase, the charged capacity exhibits only minor variation for the considered temperatures.

At first, the model is used to obtain parameters for a safe operational charging strategy. In this application scenario, an isothermal behavior has to be considered as "worst case" due to the often unknown thermal connection of the cells in system level. Fig. 12 shows the isothermal simulation results for CC/CV charging over a wide temperature and current range. For better visualization the results are interpolated between the simulated curves which
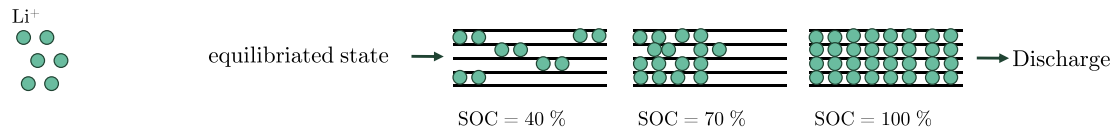
a) Room Temperature – ideal charging
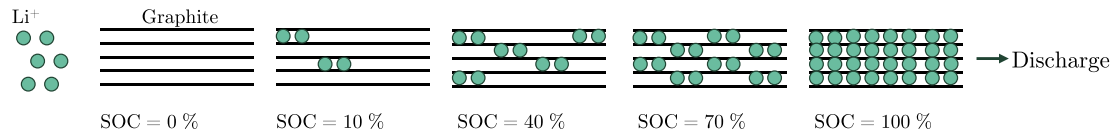
b) Low Temperature – charging to specific voltage/SOC
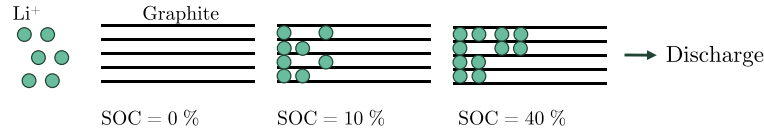
c) Low Temperature – charging from specific voltage/SOC

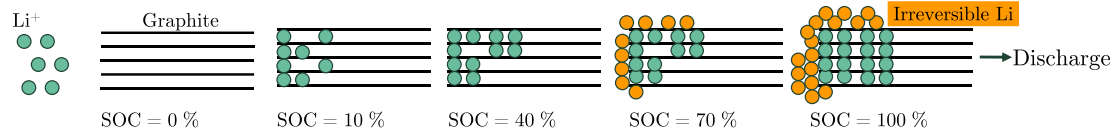**d) Low temperature –** charging over whole voltage/SOC range

Fig. 9. Schematic illustration of low-temperature aging behavior with partial charging.
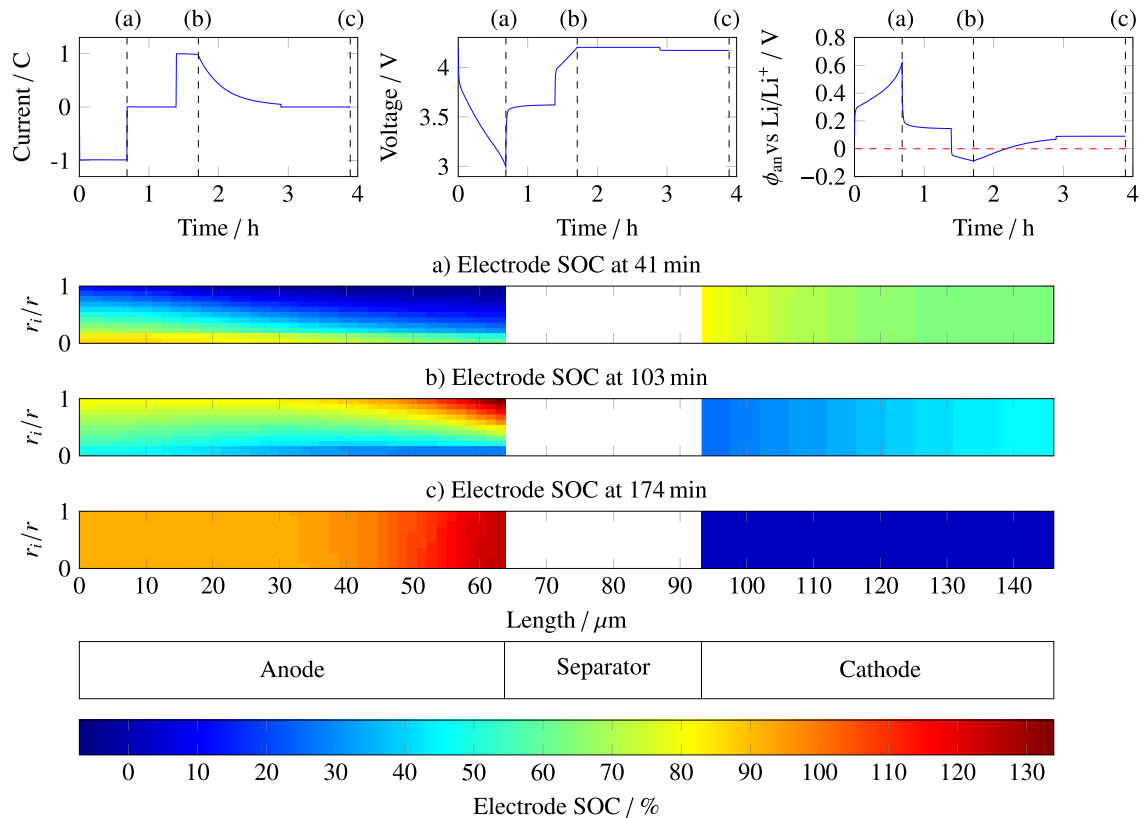

Fig. 10. Intercalated Li-concentration distribution at different points in time for a discharge−charge profile at 0 °C.
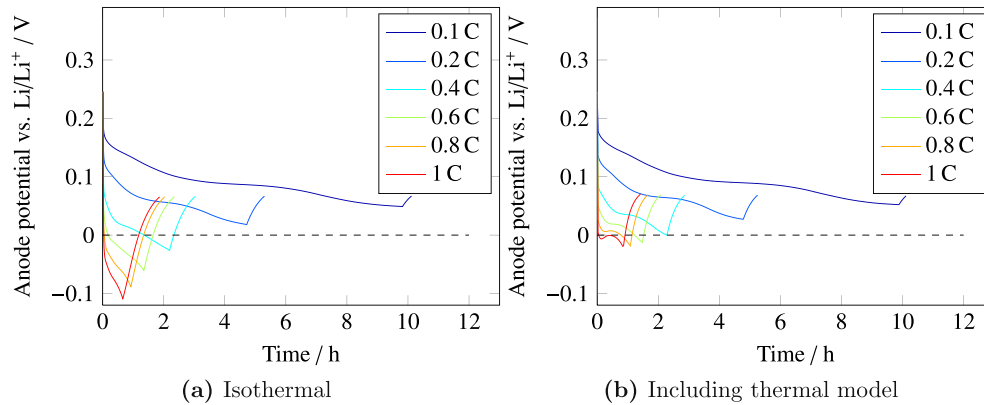
Fig. 11. Potential at anode-separator boundary for an initial cell temperature of 0 °C.
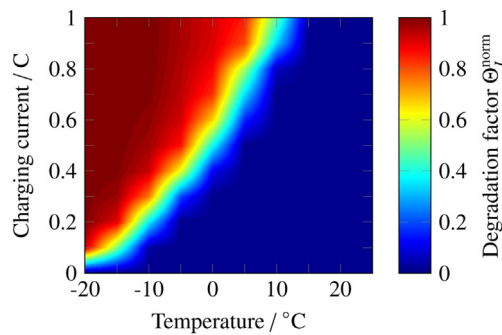

Fig. 12. Simulated degradation factor Θ_I^{norm} for a complete isothermal CC/CV charge as function of temperature and current.

are done in 5 °C and 0.1 C steps. Θ_I^{norm} is calculated and plotted over temperature and the charging current. $\Theta_I^{norm} = 1$ means that the anode potential at the anode-separator interface is below 0 V vs. Li/Li$^+$ during the whole charging process. If the anode potential stays above the critical value, the degradation factor Θ_I^{norm} is 0. For temperatures above 10 °C, no harming states are identified for currents up to 1 C. Below 10 °C the maximum possible non-harming current as a function of temperature can be identified. Additionally, only a small transition phase is observed between zero degradation and high degradation factors above 0.8. This behavior has also been observed in experiment, when switching from one to another slightly higher current.

In order to understand the real degradation behavior of single cells in a battery, the validated thermal model has to be
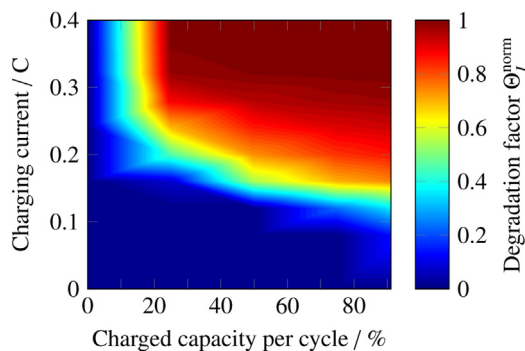

Fig. 13. Simulated degradation factor Θ_I^{norm} for partial charging at −15 °C including thermal effects.

incorporated. Significant thermal influence on the anode potential can be seen for high currents (Fig. 11). Nevertheless, temperature has only small impact on the calculated degradation maps when using current integration as there is no direct feedback of the temperature on the current and effects are only noticed when voltage goes above the defined 0 V criteria.

Assuming batteries are getting charged partially most of the time in automotive applications, not only a complete full charge has to be considered. Partial charges and different starting voltages have to be investigated as well for an optimized strategy. As already stated in the experimental section, charge capacity is a crucial factor for increased aging (cf. Fig. 8). For this case an initial SOC of 0% is chosen and a specific capacity is charged and plotted against the chosen charging current. Results are shown in Fig. 13. Concentration is fully equilibrated at the starting points. Comparing the results to Fig. 8 explains the increased aging at high charging capacities with high currents. Due to slow kinetics, a concentration build-up at the particle surface is reached which leads to a high overpotential and hence a dropping of the anode potential below 0 V vs. Li/Li$^+$. Plotting the calculated degradation factor Θ_I^{norm} for partial charges at −15 °C shows similar results by trend as for the degradation results gained in experiment. For all studies performed, the model is able to reproduce the non-harming operational parameters not only by trend but also for absolute values.

7. Conclusion

In this contribution a fully parameterized 1D + 1D electrochemical model of a lithium-ion battery cell for automotive application was presented. Model parameters were estimated by comparing simulation results to EIS experiments over a wide range of temperature and SOC. Parameters were identified by piecewise investigation of the experimental data in the frequency domain and linking the model with an optimization algorithm. The electrochemical model was coupled to a 0D thermal model and validated against galvanostatic discharge curves and realistic driving cycles with very good agreement over the whole parameterization range. Temperature increase during high-rate discharge was used for validating the thermal behavior of the coupled model. Extensive low-temperature charge measurements were carried out in order to determine the degradation behavior as function of the operational parameters temperature, current, cut-off voltage, and different charging modes. As expected, both high current and low temperature favor accelerated aging. In addition, charge capacity was identified as important parameter influencing degradation.

The model was used to predict aging effects during charging, that is lithium deposition on the anode surface. Therefore, the

anode potential at the anode-separator boundary dropping below 0 V vs. Li/Li$^+$ was taken as measure for degradation. Simulations were performed to determine non-harming operational cell parameters. For a complete CC/CV charge, the maximum allowed safe operation current for each temperature was predicted. As another crucial point, the starting SOC was examined in case of unwanted Li plating. Combining these two methods allows the implementation of the maximum possible charging current as function of temperature and SOC easily into a BMS. Comparing the semi-quantitative simulation results to experiments showed also good agreement for absolute values.

In order to characterize the plating effect on the electrochemical properties and micro-structure a first step could be to take scanning electron microscope (SEM) images of the degraded anode.

Part II of this contribution focuses on the model reduction and conversion to an on-line applicable form of the model. The reduced model can be used for a newly introduced charging mode which allows live control of the anode potential and improves charging time in a large scale [22].

Further research is ongoing for implementing a complex Li plating side reaction. Recent internal studies have shown a reversible effect to a particular capacity fade which will also be incorporated in the model.

Appendix A

Symbol and description

a^v	active specific area [m^{-1}]
a^{dl}	double layer area [m^{-1}]
A	reaction rate for Arrhenius equation
A_0	pre-exponential factor for Arrhenius equation
A_e	electrode active area [m^2]
A_{cell}	cell surface area [m^2]
c	lithium concentration [mol m^{-3}]
c_p	heat capacity [J kg^{-1} K^{-1}]
c^{ref}	electrolyte reference concentration [mol m^{-3}]
c_s^{max}	max. concentration in electrodes [mol m^{-3}]
C^{dl}	double layer capacity [F m^{-2}]
D	diffusion coefficient [m^2 s^{-1}]
E_a	activation energy [J mol^{-1}]
f	frequency [Hz]
f	activity coefficient
$f(x_i)$	model function
F	Faraday constant [As mol^{-1}]
h	convective heat transfer coefficient [W m^{-2} K^{-1})]
i	current density [A m^{-2}]
i_0	exchange current density [A m^{-2}]
i_{loc}	local current density [A m^{-2}]
I	current [A]
k	reaction rate constant [m s^{-1}]
L	length [m]
N	number of measurement points
$\dot{q}_{ohm}$	ohmic heat [W m^{-3}]
$\dot{q}_{reac}$	reaction heat [W m^{-3}]
$\dot{q}_{rev}$	reversible heat [W m^{-3}]
$\dot{Q}_{loss}$	heat loss [W]
Q_{char}	charge capacity [Ah]
Q_{dis}	discharge capacity [Ah]
r	particle radius [m]
t_+^0	transference number of lithium
R	universal gas constant [J mol^{-1} K^{-1}]
SOC	state of charge
T	absolute temperature [K]
T_{amb}	ambient temperature [K]

V_{cell}	cell volume [m^3]
x_i	fitting parameter
y_i	EIS measurement data
α	symmetry factor
χ	variable of error function
ε	porosity
ε	emissivity factor
η	overpotential [V]
$\Delta\eta_{Film}$	potential drop over SEI-film [V]
κ_l	ionic conductivity [S m^{-1}]
ϕ	potential [V]
ϕ^0	open-circuit potential [V]
ψ	stoichiometric factor anode
ν_l	thermodynamic factor
ω	weighting factor
ρ_{cell}	cell density [kg m^{-3}]
σ_{Boltz}	Stefan–Boltzmann constant [W m^{-2} K^{-4}]
σ_{cond}	electric conductivity [S m^{-1}]
σ_i	standard deviation
θ	experimental degradation factor
Θ	simulated degradation factor
ξ	stoichiometric factor cathode

Subscripts

0%	corresponds to 0% cell SOC
100%	corresponds to 100% cell SOC
an	anode
cat	cathode
i, j	indices
l	liquid
s	solid

Superscripts

ini	initial
max	maximum
norm	normalized

References

[1] Y. Ji, Y. Zhang, C.-Y. Wang, J. Electrochem. Soc. 160 (4) (2013) A636–A649.
[2] S.J. Harris, A. Timmons, D.R. Baker, C. Monroe, Chem. Phys. Lett. 485 (46) (2010) 265–274.
[3] J.M. Tarascon, M. Armand, Nature 414 (6861) (2001) 359–367.
[4] M. Doyle, T.F. Fuller, J. Newman, J. Electrochem. Soc. 140 (6) (1993) 1526–1533.
[5] T.F. Fuller, M. Doyle, J. Newman, J. Electrochem. Soc. 141 (1) (1994) 1–10.
[6] M. Doyle, J. Newman, A.S. Gozdz, C.N. Schmutz, J.-M. Tarascon, J. Electrochem. Soc. 143 (6) (1996) 1890–1903.
[7] J.P. Neidhardt, D.N. Fronczek, T. Jahnke, T. Danner, B. Horstmann, W.G. Bessler, J. Electrochem. Soc. 159 (9) (2012) A1528–A1542.
[8] S. Santhanagopalan, Q. Guo, P. Ramadass, R.E. White, J. Power Sources 156 (2) (2006) 620–628.
[9] M. Guo, G. Sikha, R.E. White, J. Electrochem. Soc. 158 (2) (2011) A122–A132.
[10] V. Boovaragavan, S. Harinipriya, V.R. Subramanian, J. Power Sources 183 (1) (2008) 361–365.
[11] A.P. Schmidt, M. Bitzer, Á.W. Imre, L. Guzzella, J. Power Sources 195 (15) (2010) 5071–5080.
[12] J.C. Forman, S.J. Moura, J.L. Stein, H.K. Fathy, J. Power Sources 210 (0) (2012) 263–275.
[13] G.M. Goldin, A.M. Colclasure, A.H. Wiedemann, R.J. Kee, Electrochim. Acta 64 (0) (2012) 118–129.
[14] P. Arora, M. Doyle, R.E. White, J. Electrochem. Soc. 146 (10) (1999) 3543–3553.
[15] M. Tang, P. Albertus, J. Newman, J. Electrochem. Soc. 156 (5) (2009) A390–A399.
[16] E. Peled, J. Electrochem. Soc. 126 (12) (1979) 2047–2051.
[17] P. Ramadass, B. Haran, R. White, B.N. Popov, J. Power Sources 123 (2) (2003) 230–240.
[18] P. Ramadass, B. Haran, P.M. Gomadam, R. White, B.N. Popov, J. Electrochem. Soc. 151 (2) (2004) A196–A203.
[19] G. Ning, B.N. Popov, J. Electrochem. Soc. 151 (10) (2004) A1584–A1591.
[20] M. Safari, M. Morcrette, A. Teyssot, C. Delacourt, J. Electrochem. Soc. 156 (3) (2009) A145–A153.

[21] M.C. Smart, B.V. Ratnakumar, J. Electrochem. Soc. 158 (4) (2011) A379–A389.
[22] J. Remmlinger, S. Tippmann, M. Buchholz, K. Dietmayer, J. Power Sources (2013) submitted for publication.
[23] W.B. Gu, C.Y. Wang, J. Electrochem. Soc. 147 (8) (2000) 2910–2922.
[24] K. Kumaresan, G. Sikha, R.E. White, J. Electrochem. Soc. 155 (2) (2008) A164–A171.
[25] K. Kumaresan, Q. Guo, P. Ramadass, R.E. White, J. Power Sources 158 (1) (2006) 679–688.
[26] M. Doyle, J.P. Meyers, J. Newman, J. Electrochem. Soc. 147 (1) (2000) 99–110.
[27] K.M. Shaju, G.V. Subba Rao, B.V.R. Chowdari, J. Electrochem. Soc. 151 (9) (2004) A1324–A1332.

[28] M.D. Levi, D. Aurbach, J. Phys. Chem. B 101 (23) (1997) 4641–4647.
[29] J.C. Lagarias, J.A. Reeds, M.H. Wright, P.E. Wright, SIAM J. Optim. 9 (1998) 112–147.
[30] L.O. Valoen, J.N. Reimers, J. Electrochem. Soc. 152 (5) (2005) A882–A891.
[31] W. Fang, O.J. Kwon, C.-Y. Wang, Int. J. Energy Res. 34 (2) (2010) 107–115.
[32] O.J. Kwon, C.-Y. Wang, Lithium Deposition in the Anode of Automotive Li-ion Batteries, Meeting Abstracts MA2009-02(8), 2009, p. 544.
[33] O.J. Kwon, W. Fang, C.-Y. Wang, Lithium Deposition in the Anode of an Automotive Li-Ion Battery: Experiments and Modeling, Meeting Abstracts MA2010-03(1), 2010, p. 279.